THE UNIVERSITY OF

WARWICK

In-plane and out-of-plane measurements of Rayleigh waves using EMATs for characterising surface cracks

M.H. Rosli, R.S. Edwards*, Y. Fan

Department of Physics, University of Warwick, Coventry, CV4 7AL, UK

Abstract

Electromagnetic acoustic transducers (EMATs) have been used to measure the properties of Rayleigh waves in the vicinity of defects propagating at different angles to the sample surface, which are more representative of real defects than slots machined normal to the surface. Transmission measurements show that one must consider the angle of the defect when choosing a depth calibration curve. We propose a procedure for crack characterisation (depth, angle) that considers transmission alongside measurements of both the in-plane and out-of-plane velocity components of the Rayleigh wave in the near-field of a defect, where the signal is enhanced due to constructive interference of incident and reflected wavemodes, and/or mode conversion. This procedure uses image analysis of B-Scans alongside the ratio of the enhancement in the in-plane to the out-of-plane components to characterise the angle. Once this is known the correct transmission depth calibration curve can be used. The procedure shows very good agreement between the measured and the actual slot characteristics on test samples.

---

*Corresponding author

Email address: `r.s.edwards@warwick.ac.uk` (R.S. Edwards)

1. Introduction

The presence of surface breaking crack in metals, such as rolling contact fatigue (RCF) and stress corrosion cracking (SCC), is known to pose many risks to the environment in which it is present [1, 2]. It is essential that there is a fast and reliable method to quantify the severity of the cracks. Ultrasonic testing (UT) is one of the non-destructive testing (NDT) techniques suitable for this purpose. Current UT techniques used for RCF consist of a wheel probe containing a piezoelectric transducer, generating bulk waves and measuring reflections from surface defects [3]. This, however, is slow and can underestimate the depth of serious defects when they fall in the shadow of a shallow defect [3]. Recent work has considered instead a measurement of the transmission of broadband Rayleigh waves, with transmission decreasing as the defect depth increases [4]. The technique has several potential advantages over conventional UT methods, including the potential for higher speed testing, and the deepest defect within a cluster dominating the transmission.

Calibration of techniques is typically done using either flat bottomed or side drilled holes, or slots machined normal to the sample surface. However, this does not always replicate real defects. For instance, in rail inspection the geometry of the defect can give information about the severity and the remedial action required; inclined cracks may indicate RCF cracking, which typically grows at about 25° to the rail surface [2].

1.1. Interaction of Rayleigh waves and surface defects

The interaction of Rayleigh waves with surface cracks has been studied by several authors [4–7]. Rayleigh waves have various properties which make them suitable for characterising surface cracking; attenuation of the wave is generally small when compared to propagation of bulk waves within a material, and most of the wave energy is confined within a wavelength from the sample surface [5].

For slots which are machined normal (i.e. at 90°) to the sample surface, Viktorov relates the period of the oscillating pattern observed in the calculated reflection coefficients, R, and transmission coefficients, T, with the crack depth [5], while Mandelsohn investigated the scattering of surface waves by a surface-breaking crack in a two dimensional geometry, showing an oscillating pattern in both the in-plane and out-of-plane components of R [6]. The transmission of Rayleigh waves in the region of 90° defects has been studied by several authors, showing a drop in transmitted signal amplitude as the crack depth increases [4]. For broadband waves, such as those generated by the EMATs here, a measure of the transmitted frequency content can also give a measure of the crack depth [4, 7].

Recently, a number of authors have investigated the enhancement of Rayleigh waves at a very close proximity to a 90° surface crack [8–11], which can be used as an indication of the crack position. For 90° defects, this increase in signal amplitude can be attributed to constructive interference between the incident Rayleigh wave and the reflected Rayleigh and mode-converted surface skimming longitudinal wave [10, 11]. These measurements show a larger enhancement in the in-plane motion than the out-of-plane

3

motion, due to the contribution of the longitudinal mode being primarily in-plane.

However, whilst these machined slots are a good initial approximation of surface defects, they do not necessarily give a full picture of the transmission and enhancement in the region of realistic defects. Firstly, the signal enhancement measured may depend on crack roughness and geometry [8]. Secondly, and perhaps more importantly, the reflection coefficient varies with angle [5], and it has been shown for laser generation and detection [12] and for narrowband contact UT measurements [13] of surface waves that the angle of the defect to the surface affects the transmission. Hence it is important to measure the angle of a surface-breaking defect, and use this to choose a correct depth calibration. The time delay of a Rayleigh wave passing underneath a crack is one possible measure of the crack inclination [12, 14].

Numerous UT methods have been developed for NDT, adopting the conventional contact (e.g. piezoelectric) transducer approach, using non-contact transducers, or a combination of both [7, 13, 15, 16]. In the contact approach, contact with the sample under test and the use of couplant is required. With non-contact transducers the transducer can be placed at a standoff from the sample [17]. However, piezoelectric transducers are more efficient than EMATs, and the decision to use one approach over the other should be justified by the specific needs [17].

A measurement system using electromagnetic acoustic transducers (EMATs) is reported here for full characterisation of surface cracks in electrically conducting materials. The system measures transmission of surface ultrasonic waves, detecting the in-plane and out-of-plane velocity components sepa-

rately as the wave propagates in the vicinity of a surface crack. In section 2 the EMATs and experimental set-up are described. In section 3.1 we give transmission calibrations for a range of defect angles. Finally, in section 3.2 we first consider initial classification of the defect using qualitative analysis of B-scan images produced during scans of a sample, and then consider the ratio of the in-plane and out-of-plane components of the signal enhancement in the near field, and how these can be used to gauge the defect angle.

2. Experimental details

The behaviour of the Rayleigh wave in the near-field and far-field of a surface-breaking defect have been investigated both experimentally and using a finite element method (FEM) model, in order to design a system capable of characterising both the depth and angle of a defect relative to the surface.
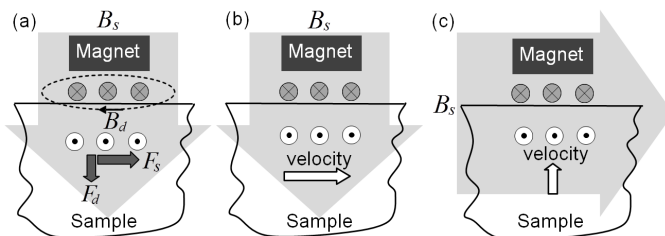
2.1. Scanned EMAT System

Figure 1: Generation and detection mechanism of an EMAT; (a) Lorentz force generation, (b) in-plane receiver, (c) out-of-plane receiver. B_s is shown by the large arrow.

The generation mechanism of an EMAT may be via the Lorentz force, magnetization-force, and/or magnetostriction, depending on the sample properties [17–19]. The samples used in these experiments are aluminium, with

the top 3 mm of aluminium removed [20]. For generation of ultrasonic waves we have used a linear EMAT (linear coil consisting of 8 turns of 0.315 mm diameter wire wrapped around a cylindrical permanent magnet). The coil and the magnet are arranged as shown in Figure 1(a). A current is pulsed through the coil and, when held close to the aluminium sample, induces a mirror current $\vec{J}$ within the skin depth of the sample. The mirror current will interact with the static magnetic field from the magnet, $\vec{B}_s$, and the dynamic magnetic field $\vec{B}_d$ from the current pulse, giving a Lorentz force, $\vec{F}$ [19]:

$$\vec{F} = \vec{F}_s + \vec{F}_d = \vec{J} \times (\vec{B}_s + \vec{B}_d). \tag{1}$$

which in turn generates ultrasonic waves within the sample [17].

For detection, the directional sensitivity is determined by the magnetic field and coil design arrangement [19]. Figure 1(b) shows a design of EMAT using a linear coil which is sensitive primarily to the in-plane particle velocity, while Figure 1(c) shows a detection EMAT sensitive primarily to the out-of-plane velocity.
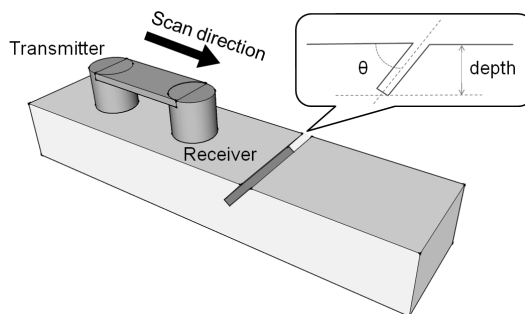

Figure 2: Experimental set-up. The transmitter and receiver EMATs are scanned towards a slot. The slot inclination to the surface, θ, and vertical depth, d, are shown in the inset.

In all experiments the transmitter and receiver EMATs are held 150 mm apart in a "pitch-catch" arrangement, as illustrated in Figure 2. The liftoff is fixed at 100 μm, giving a good signal to noise ratio [21]. Surface cracks are simulated on aluminium bars of dimensions $60 \times 60 \times 900$ mm by machining slots across the bar-width at specific angles, θ, and depths d, as illustrated in the inset to Figure 2; d is varied from 1 to 20 mm for $\theta = 45°$ and $90°$, and θ is varied from $15°$ to $90°$ for depths of 3 and 5 mm. These depths were chosen such that they give a reasonable transmitted amplitude when compared to the generated Rayleigh wave with a central wavelength of 12.6 mm.

The holder containing the transmitter and receiver EMATs is scanned along the sample, as shown in Figure 2, using an X-Y stage with 0.1 mm step increments, with measurements detecting either the in-plane or out-of-plane velocities. LabVIEW and a PicoScope oscilloscope were used to average and record signals in the time-domain. A set of measurements are made on a clear section of sample to give a reference signal amplitude which can be compared to changes in signal amplitude due to the presence of a defect. During a scan, negative distance indicates that the receiver and transmitted are on the same side of the slot.

2.2. Finite Element Method model

Rayleigh wave interactions are modelled using PZFlex, a FEM program, which allows extension to a wider range of depths and angles than is available experimentally [11, 22]. The slot width for the samples extends across the full width of the bar, therefore the FEM model can be reduced to a two dimensional model. The contribution of the dynamic and static generation forces depend on the form of the pulsed current, hence the time information

from a measurement of the current is used to model the generation pulse.

The modelled sample has an element side length of 129μm, with the side and bottom boundaries set as absorbing to minimise reflections. The slot is defined as a rectangular void of 1 mm width, inclined at an angle θ and depth d. 90°, 45° and 22.5° slots are modelled with d ranging from 1 mm to 20 mm, while 3 mm and 5 mm slots were modelled with θ ranging from 15° to 165° at approximately 10° increments. The generation point has an effective width of 2 mm and the in-plane and out-of-plane velocities are recorded at each node from 150 mm to 250 mm away from the generation point.

Figure 3 shows the normalised fast Fourier transform (FFT) of Rayleigh waves from the experiment and the model. The generated Rayleigh wave is broadband, centred at about 238 kHz, and experiment and model show good agreement.
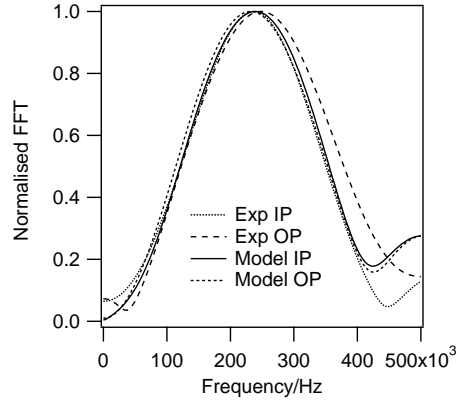

Figure 3: Normalised Fast Fourier Transform of Rayleigh waves from experiment and model. IP and OP correspond to the in-plane and out-of-plane components.

8

2.3. Velocity components of the Rayleigh wave

EMATs are velocity sensors [19]. The particle velocities for a Rayleigh wave in the in-plane, V_x, and out-of-plane, V_z, components can be calculated from the displacements (U_x and U_z) given in Viktorov [5] as follows;

$$V_x = A\omega k_R \left(e^{-qz} - \frac{2qs}{k_R^2 + s^2} e^{-sz} \right) cos(k_R x - \omega t) \tag{2}$$

$$V_z = A\omega q \left(\frac{2k_R^2}{k_R^2 + s^2} e^{-sz} - e^{-qz} \right) sin(k_R x - \omega t) \tag{3}$$

where k_R, k_l and k_t are the wave numbers of Rayleigh, longitudinal and shear waves respectively, $q = \sqrt{k_R^2 - k_l^2}$, $s = \sqrt{k_R^2 - k_t^2}$, A is a constant and x and z are the in-plane (x axis) and out-of-plane (z axis) positions.
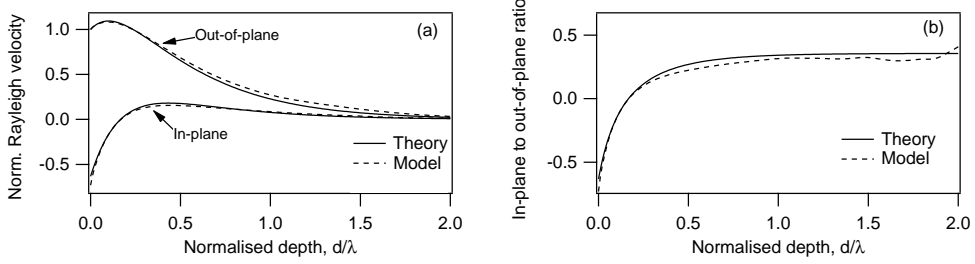

Figure 4: Calculation and FEM results showing the variation of Rayleigh wave velocities with normalised depth d/λ. (a) Maximum Rayleigh wave velocities, (b) the velocity ratio as a function of normalised depth.

The velocities are normalised to the out-of-plane velocity on the surface $V_{z(z=0)}$ and plotted as a function of normalised depth, d/λ, and shown in Figure 4(a). Corresponding velocity values have also been recorded from the FEM model, showing very good agreement between the model and analytical values. In Figure 4(b) the ratio of the in-plane to the out-of-plane components are shown for the same depth range, highlighting that the variation is significant until a depth of $d \approx 0.4\lambda$, before the ratio stabilises.

9

3. Experiment and FEM results

The analysis of each scan is divided into measurements in the far-field and near-field regions of angled defects. Measurements of the transmission are made in the far-field, where both EMATs are at least 5 wavelengths from the slot (with the wavelength taken as the central wavelength, 12.6 mm). At this distance the Rayleigh wave has stabilised following interaction with the slot and the transmission coefficient can reliably be measured. Near-field measurements are made when the receiver is very close to the slot, and signal enhancement is observed [9, 10].
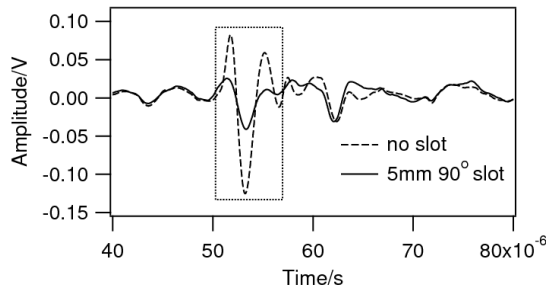
3.1. Far-field measurements

Figure 5: A-scans of the out-of-plane measurements of a sample with a 5 mm deep 90° crack, and over a section with no crack. The dotted box indicates the Rayleigh wave.

A slot on the surface will act like a low-pass filter to the incident Rayleigh wave, where the cut-off frequency is related to the slot's normalised depth [4]. For a broadband Rayleigh wave, the depth of a slot can then be gauged from changes in the amplitude and frequency content by comparing a reference signal, measured on a section of a sample clear of defects, to the signal transmitted through a defective region (Figure 5). Here, we analyse changes in the

10

time-domain signals by measuring the peak-peak amplitude of the incident (A_i) and transmitted (A_t) Rayleigh waves and calculating the transmission coefficient, C_T,

$$C_T = \frac{A_t}{A_i}. \tag{4}$$

This contains a contribution from all the frequencies present, and is calculated for the in-plane and out-of-plane components.

Figure 6 shows C_T for the in-plane and out-of-plane velocity components measured experimentally, as a function of slot depth, for 90°, 45° and 135° (opposite scanning direction to 45°) slots. The results for 135° slots show very close agreement with the 45° plot. These curves can be used as a depth calibration. A fit is shown for each set of data by assuming an exponential decay of peak-to-peak amplitude with depth (equations 2 and 3).
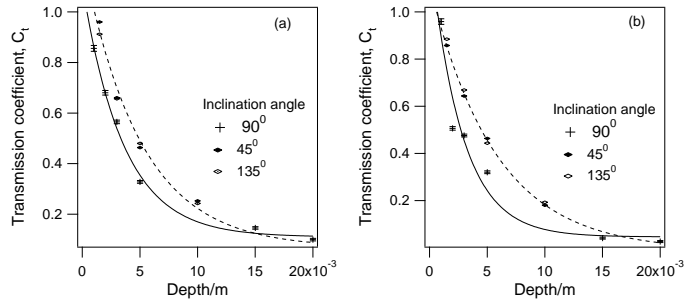

Figure 6: In-plane (a) and out-of-plane (b) depth calibration curves from experiment.

Clearly, θ is affecting the transmission measurement. We observe differences between the calibration curves produced for 90° and angled slots in both the experiment and models. This could lead to significant errors if the wrong calibration curve is applied; for example, if a 45° slot was characterised using the 90° curve and the measured C_T was 0.4, the slot depth

would be underestimated by $\approx$ 2.3 mm. However, from the modelled results the difference between the 22.5° and 45° calibration curves is very small. In this case, a 22.5° slot can be characterised using the 45° calibration curve, or vice versa. We cannot blindly rely on the 90° depth calibration curve to accurately characterise all defects.

The variation of C_T with crack angle for 3 mm deep slots is shown in Figure 7. This is approximately symmetric about 90°, with angles greater than 90° measured by scanning the corresponding acute angle in the opposite direction. For angles of less than 45° the variation in C_T is minimal.
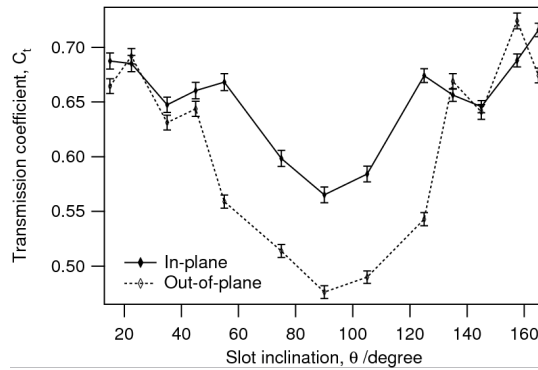

Figure 7: Variation of transmission coefficient with θ for 3 mm deep slots.

3.2. Near-field measurements

The transmission coefficient measurements show that a method is required to identify the orientation of a defect in order to apply the correct calibration. For initial classification of a defect into 'inclined' / 'close-to-90°' we use image analysis of scan results.

Figure 8 shows B-scan representations of the experimental scans (out-of-plane) of samples containing 3 mm deep defects at three different inclinations,

$\theta = 22.5°$, $90°$ and $157.5°$. A-scans recorded at each position in a scan are stacked together to form the B-scan, with the amplitudes of the waves given by the colour scale. The y-axis shows the distance between the receive EMAT and the slot, while the x-axis gives the arrival time, and each wave mode can be identified by its arrival time as a function of scan position [11, 12, 14]. The incident Rayleigh wave arrives at about $52\mu s$.
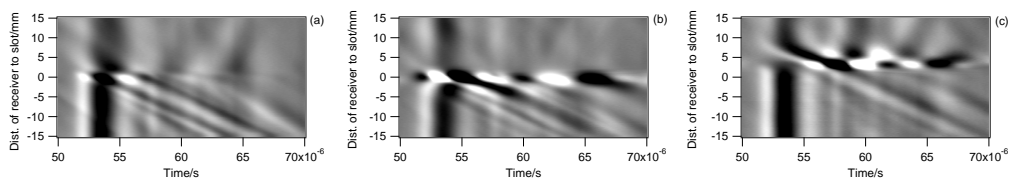

Figure 8: B-scans of the out-of-plane measurements showing the enhancement pattern from 3 mm slots of inclinations (a) $\theta= 90°$, (b) $\theta= 22.5°$, (c) $\theta= 157.5°$.

There is a clear difference in the near-field between the scans. Firstly, we can consider the changes in arrival time of a Rayleigh wave transmitted underneath a defect. These have been calculated for incident, reflected and transmitted Rayleigh waves, plus mode-converted bulk wavemodes, in [11, 12, 14], for normal and angled defects. For the 157.5° defect (Figure 8(c)) a significant delay in the Rayleigh wave arrival time is seen in the near-field following transmission. This delay time is governed by the defect length and inclination, and could be used for defect characterisation [23].

The enhancement pattern observed for each angle is also strikingly different, and can be used to position and characterise the defect. For a 90° slot this enhancement pattern is well understood; in Figure 8(a) the incident and reflected Rayleigh waves can be seen interfering constructively close to the defect (with a surface skimming longitudinal wave contributing signifi-

13

cantly to the in-plane enhancement [10]). However, in Figures 8(b) & (c) the signal enhancement is stronger and has a different time dependence, forming an alternating black and white pattern. The pattern produced by the 90° slot extends to about 58 μs, while the 22.5° slot produces an enhancement pattern that spans to the end of the time scale shown. Furthermore, the enhancement has a clear dependence on angle.

Image analysis of these B-scans gives some information about the defect. Firstly, the position of the slot can be determined from the enhancement. Secondly, a distinction between near-90° slots and inclined slots can be made. Finally, the orientation of the slot tip, i.e. whether it is facing (acute angle) or opposing (obtuse angle) the direction of travel of the incident Rayleigh wave can be determined. An image classification program using machine learning has been developed to extract this information from a B-scan, with initial results giving a 100% accuracy in identification for a small data set [24].
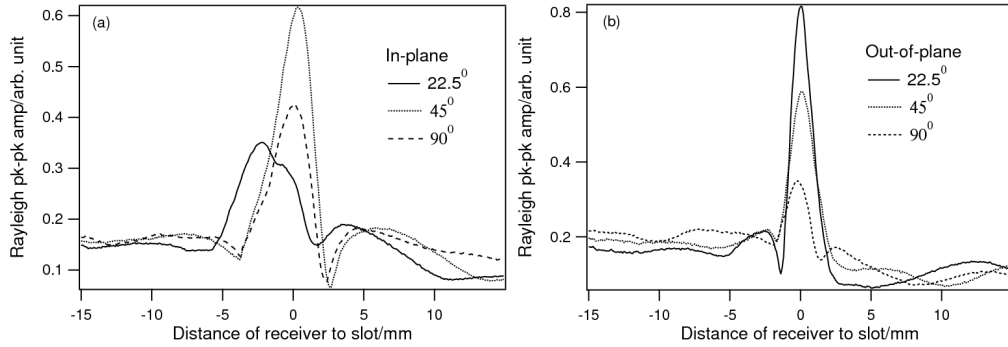

Figure 9: Variation of the Rayleigh wave amplitude with the distance relative to 3 mm slots of different inclinations.

Following the B-scan analysis, further analysis of the near-field enhancements can be used to give an approximate measure of the angle of slots in

14

the range $0° \leqslant \theta \leqslant 90°$. To quantify the enhancement the peak-to-peak amplitude of the Rayleigh wave is measured at each scan point and plotted as a function of scan distance, as shown in Figure 9 for 3 mm deep slots. A new parameter, the enhancement factor F_E, is introduced as the measure of the enhancement, by normalising the enhanced amplitude, A_E, at the peak by the reference amplitude A_i;

$$F_E = \frac{A_E}{A_i}. \tag{5}$$

F_E is calculated for both the in-plane and out-of-plane measurements, which have different angle-dependent behaviour, as shown in Figure 9. Figure 10 shows F_E as a function of depth for 90° and 45° slots (the lines are given as a guide-to-the-eye to show the general trend in the data). For slot depths > 2 mm the 45° slots show much larger values of F_E, of up to 5.7 times the incident amplitude in the in-plane and 4.6 in the out-of-plane measurements for 10 mm deep slots.
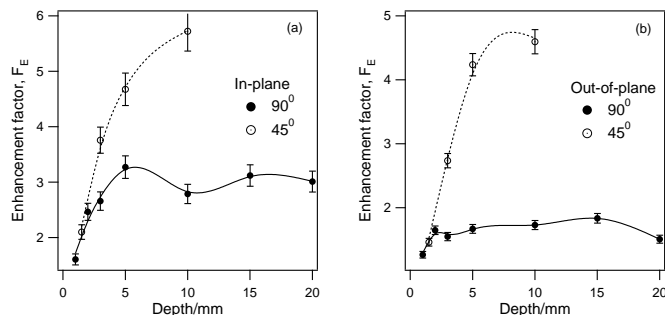

Figure 10: Enhancement factor F_E as a function of depth for 90° and 45° slots, for (a) in-plane, (b) out-of-plane experimental measurements. The lines are a guide to the eye to show the trend of the data.

In Figure 10 the value of F_E for both slots increases rapidly as the depth

15

increases from zero, and for the 90° slots settles at a depth of around 5 mm. For the central wavelength of 12.6 mm, this corresponds to $d/\lambda = 0.40$. This implies that, for the 90° slots, the interaction occurs primarily within a fraction of a wavelength of the surface.
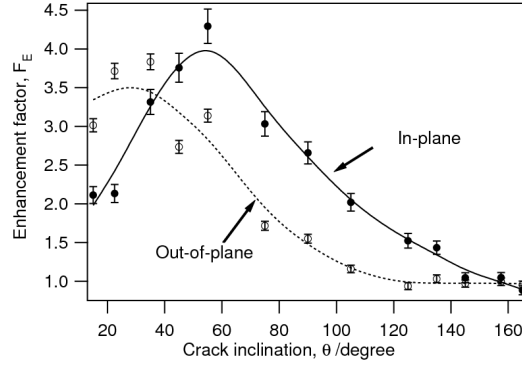

Figure 11: Variation of enhancement factor F_E with crack angle.

F_E for both components is plotted as a function of θ for 3 mm deep slots in Figure 11, showing the expected larger in-plane enhancement at 90° [10]. For angles < 15°, difficulties in producing reliable samples and models with high enough node densities precludes an extension of the discussion to less than 15°. Both components increase to a maximum below 90° before decreasing to a value of 1 at large θ values, where the Rayleigh wave is relatively undisturbed by the presence of the defect. However, for real defects the exact enhancement will depend on the reflectivity, and a smaller overall enhancement may be observed due to the finite size of the detection EMAT. In this case it can be beneficial to study the ratio of the in-plane $(F_{E(IP)})$ to the out-of-plane $(F_{E(OP)})$ enhancements, F_{ER}, as both are affected by the crack

16

characteristics;

$$F_{ER} = \frac{F_{E(IP)}}{F_{E(OP)}}.\tag{6}$$

This ratio was calculated and plotted as a function of θ for slots of vertical depth 3 mm and 5 mm for both model and experiment, shown in Figure 12. A dashed line is given as a guide to the eye, but is not intended to be an accurate fit. The plot shows that the F_{ER} values are less than 1 in the small angle region (15°-35°) and increase gradually above 1 for angles greater than 45°; the out-of-plane component is found to be more dominant than the in-plane in the small angle region, while the opposite is true outside this range.
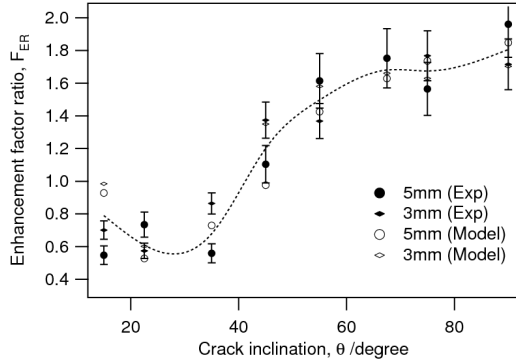

Figure 12: Variation of enhancement factor ratio, F_{ER} with crack inclination, θ. The dashed line is a guide to the eye only.

In order to understand this behavior, one can first consider the behaviour of Rayleigh waves incident on a wedge [25, 26]. Within the wedge the local thickness varies depending on the position relative to the tip. As the Rayleigh wave here interacts with an angled defect, some of the wave will be transmitted underneath the slot, while the rest will be trapped within the wedge formed by the defect. Considering the change of the frequency-thickness, from the full bar thickness to the local thickness within the angled defect,

17

one would expect to see conversion to a Lamb-like wave, with the fundamental Lamb wave modes ($S0$ and $A0$) of interest in this frequency-thickness range. The velocities of these modes depend on the frequency-thickness product [27], with the $A0$ mode arriving approximately within the time window set to measure the Rayleigh wave peak-peak amplitude [25].
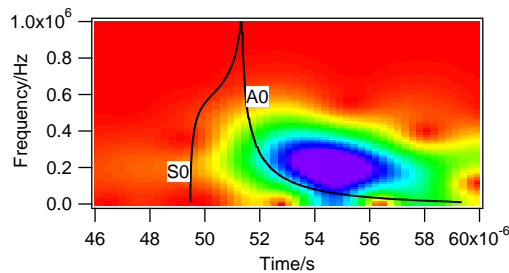

Figure 13: Spectrogram of the out-of-plane experimental signal at the tip of the 15°, 5 mm deep slot. Solid lines show the calculated arrival times of the $S0$ and $A0$ modes.

Evidence of mode conversion from a Rayleigh wave to an $A0$-like mode is given by the spectrogram in Figure 13, for the A-scan recorded by the out-of-plane EMAT very close to the opening of the 15°, 5 mm deep slot, with the calculated arrival times of the $S0$ and $A0$ modes shown as lines [25, 27]. At low frequencies the out-of-plane signal is dominated by a mode arriving close to the expected arrival time of an $A0$ mode, and some dispersion is clear. For the small frequency-thickness product close to the defect tip one would expect to see a significant out-of-plane component in the $A0$ mode, whereas the in-plane component would be smaller [27]. At the tip the $A0$-like mode will be reflected, with interference plus the relative magnitudes of Rayleigh compared to Lamb waves giving the larger out-of-plane signal enhancement. As the angle of the crack increases we return to the bulk-

wave picture close to 90°, with enhancement again mainly due to interference of incident and reflected Rayleigh waves with the mode-converted surface skimming longitudinal mode, with the in-plane enhancement dominating.

Comparing measured values of F_{ER} to the calibration in Figure 12 will give an approximate value of θ to within about 10°. The estimate is sufficient to give the correct depth calibration curve to use for a depth measurement.

4. Procedure for characterising surface cracks

In this section we describe a procedure (Figure 14) which has been developed to use the far-field and near-field measurements to characterise surface cracks, finding their vertical depth, orientation of the crack (i.e. whether the crack tip is facing the incoming Rayleigh wave or opposing it), and a rough estimate of the crack angle to the surface. The scan of the sample, which can either be done separately for the in-plane and out-of-plane measurements, or by using a trolley holding two receiver EMATs, is set such that the receiver will be initially in the far-field, is then scanned over a crack (near-field) and then reaches the far-field region on the other side of the crack. From the scan, several analyses are done in parallel; B-scan analysis (image analysis), and Rayleigh wave peak-peak amplitude analysis in both the near (enhancement) and far-field (transmission) regions.

The B-scan analysis gives the position of the crack, along with an indication of whether the crack is in the near-90° range or inclined to the surface. For a near-90° crack, the depth estimate can be done directly from C_T, with characterisation using the 90° depth calibration curve (Figure 6). For inclined cracks, we first determine the orientation of the crack using the B-scan. If
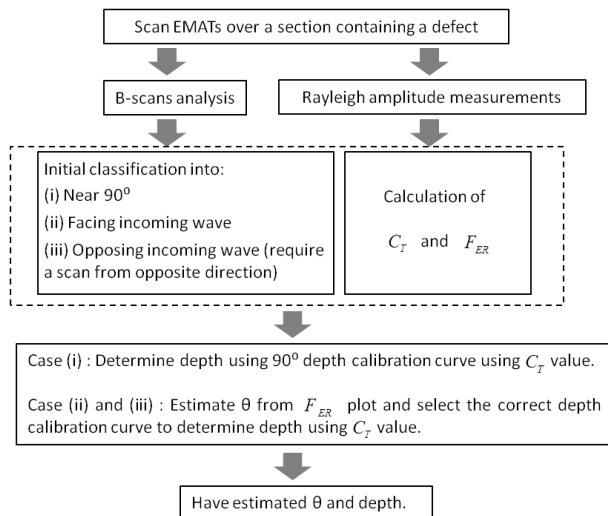
19

Figure 14: Procedure for characterising surface cracks.

the B-scan indicates that the crack tip is facing the incoming Rayleigh wave (case (ii)), we can proceed directly to calculating F_{ER}. However, if the B-scan indicates that the crack is inclined away from the Rayleigh wave travel direction, the sample is scanned in the opposite direction to meet the condition in case (ii). Automatic classification of B-scans using machine learning can speed up the classification process and reduce human dependence [24]. The value of F_{ER} is then used to estimate θ, and a correct depth calibration curve can be used to estimate the depth.

4.1. Testing on two unknown machined slots

The procedure has been tested on two machined slots of depths 4±0.2 mm (at $30° \pm 3°$) and 7 ± 0.2 mm (at $45° \pm 3°$), labelled as Crack 1 and Crack 2. The depths and angles of these defects were not measured prior to analysis. The transmitter and receiver EMAT were scanned initially in one direction, with the scan distance measurement reset prior to scanning crack 2. B-scan

analysis (Figure 15) indicates that both cracks are angled-defects, with Crack 1 facing the direction of travel of the incident Rayleigh wave while Crack 2 is opposing. A second scan was made over Crack 2, moving in the opposite direction. Figure 16 shows the normalised Rayleigh wave amplitude plotted against scan distance for the cases when $\theta < 90°$.
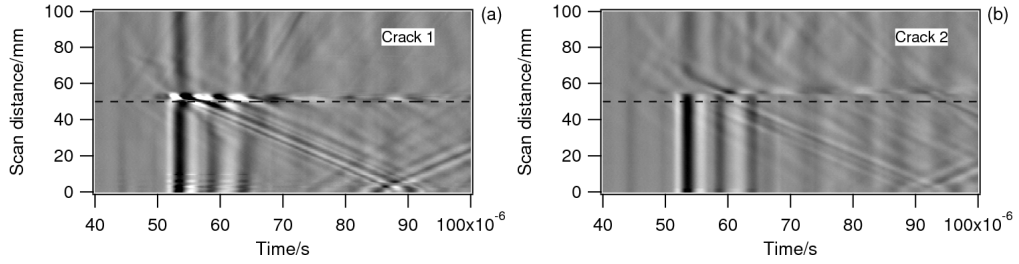

Figure 15: B-scans using out-of-plane receiver in the first scanning direction. The dotted line indicates the position of the slots.
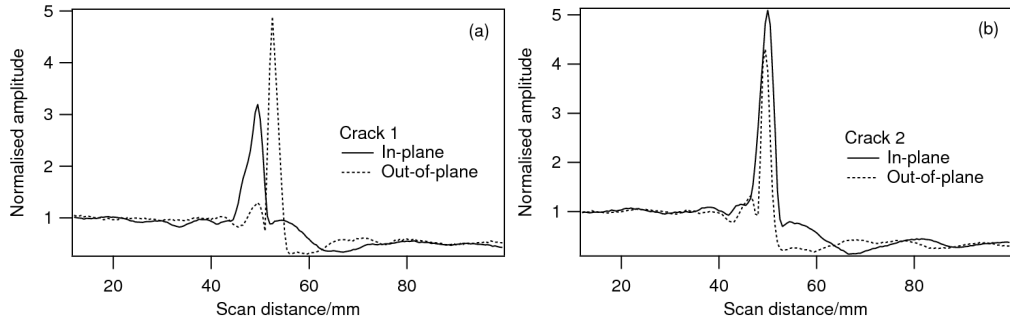

Figure 16: Normalised peak-peak amplitude of the Rayleigh plotted as a function of the scan distance, for the scans where $\theta < 90°$.

For Crack 1 (Figure 16(a)), the enhancement has $F_{E(IP)} = 3.20$ and $F_{E(OP)} = 4.89$. For Crack 2 (Figure 16(b)), the enhancement has $F_{E(IP)} = 5.10$ and $F_{E(OP)} = 4.30$. Hence F_{ER} for Crack 1 is 0.65, while for Crack 2 it is 1.18. θ for Crack 2 is estimated as 45° using figure 12, while for Crack

21

1 there are two possible values, 20° and 34°, with a higher likelihood for 34° from the magnitude of the enhancements. The depths of both cracks can therefore safely be estimated using the 45° calibration, giving depths of 4.5 ± 0.6 mm for Crack 1 and 7.4 ± 0.9 mm for Crack 2. This shows an excellent agreement between the values measured using the procedure and using visual techniques.

5. Conclusions

Measurements of the in-plane and out-of-plane Rayleigh wave components confirm that the transmission of a Rayleigh wave underneath a surface-breaking defect is affected by both the slot angle and depth. Therefore, the assumption that a surface crack can be simulated by a machined slot which propagates perpendicularly to the surface is not always accurate. In order to accurately characterise the slot depth using the transmission coefficients the inclination of the slot needs to be determined before an appropriate calibration curve can be selected. Image analysis of B-scans in the near-field indicates whether a slot is approximately normal or inclined to the surface, and provides information on the orientation of the slot relative to the direction of the Rayleigh wave. Calculation of the ratio of the enhancement factors of the in-plane to out-of-plane Rayleigh wave velocity components, F_{ER}, can then be used to approximate the slot inclination. The technique described here has been tested on two machined slots. The results show a good agreement with measurements by eye and confirms the viability of this technique for characterising surface cracks.

A scanning system for online measurements will incorporate several re-

ceive EMATs, giving both in-plane and out-of-plane measurements in a single scan, so that information from both can be acquired in parallel. Provided that a preliminary reference measurement is made over an clear section of the sample, analysis can be done during a scan to produce a real-time characterisation of surface cracks.

References

[1] R.A. Cottis, *Guides to Good Practice in Corrosion Control: Stress Corrosion Cracking*, HMSO (2000)

[2] Railtrack Plc., *Rolling Contact Fatigue in Rails; A Guide to Current Understanding and Practice* (2001)

[3] D. Hesse and P. Cawley, *Review of Progress in Quantitative Nondestructive Evaluation* **25A&B** (AIP Conference Proceedings Vol. 820) 1593-1600 (2006)

[4] R.S. Edwards, S, Dixon and X. Jian, *Ultrasonics* **44(1)** 93-98 (2006)

[5] I.A. Viktorov, *Rayleigh Waves and Lamb Waves-Physical Theory and Application*, Plenum Press, New York (1967)

[6] D.A. Mendelsohn, J.D. Achenbach and L.M. Keer, *Wave Motion* **2(3)** 277-292 (1980)

[7] R.S. Edwards, S. Dixon and X. Jian, *NDT & E International* **39(6)** 468-475 (2006)

[8] S. Dixon, B. Cann, D.L. Carroll, Y. Fan and R.S. Edwards, *Nondestructive Testing and Evaluation* **23(1)** 25-34 (2008)

[9] J.L Blackshire and S. Sathish, *Applied Physics Letters* **80(18)** 3442-3444 (2002)

[10] R.S. Edwards, X. Jian, Y. Fan and S. Dixon, *Applied Physics Letters* **87(19)** 194104 (2005)

[11] X. Jian, S. Dixon, N. Guo and R. Edwards, *Journal Of Physics D - Applied Physics* **101(6)** 064906 (2007)

[12] B. Dutton, A.R. Clough, M.H. Rosli and R.S. Edwards, *NDT & E International* **44(4)** 353-360 (2011)

[13] V.K. Kinra and B.Q. Vu, *Journal of the Acoustical Society of America* **79(6)** 1688-1692 (1986)

[14] C.Y. Ni, Y.F. Shi, Z.H. Shen, J.A. Lu and X.W. Ni, *NDT&E International* **43(6)** 470-475 (2010)

[15] I. Baillie, P. Griffith, X. Jian and S. Dixon, *Review Of Progress In Quantitative Nondestructive Evaluation* **28A&B** (AIP Conference Proceedings Vol. 1096) 1711-1718 (2009)

[16] A. Moura, A.M. Lomonosov and P. Hess, *Journal of Applied Physics* **103(8)** 084911 (2008)

[17] S.B. Palmer and S. Dixon, *Insight* **45(3)** 211-217 (2003)

[18] M. Hirao and H. Ogi, *EMATs for Science and Industry*, Kluwer Academic Publishers (2003)

[19] X. Jian, S. Dixon, K. Quirk and K.T.V. Grattan, *Sensors & Actuators A - Physical* **148(1)** 51-56 (2008)

[20] S. Dixon, C. Edwards and S.B. Palmer, *Insight* **40(9)** 632-634 (1998)

[21] J.P. Morrison, S. Dixon, M.D.G. Potter and X. Jian, *Ultrasonics* **44** E1401-E1404 (2006)

[22] X. Jian, Y. Fan, R.S. Edwards and S. Dixon, *Journal of Applied Physics* **100(6)** 064907 (2006)

[23] A.R. Clough, B. Dutton and R.S. Edwards, *Review Of Progress In Quantitative Nondestructive Evaluation* **30A&B** 137-144 (2011)

[24] M.H. Rosli, R.S. Edwards, B. Dutton, C.G. Johnson and P.T. Cattani, *Review Of Progress In Quantitative Nondestructive Evaluation* **29A&B** (AIP Conference Proceedings Vol. 1211) 1593-1600 (2010)

[25] R.S. Edwards, B. Dutton, A.R. Clough and M.H. Rosli, *Applied Physics Letters* **99(9)** 094104 (2011)

[26] R.J. Blake and L.J. Bond, *Ultrasonics* **28(4)** 214-228 (1990)

[27] J.L. Rose, *Ultrasonic Waves in Solid Media*, Cambridge University Press(1999)